

Visualization of water vapour flow in a packed bed adsorber by near-infrared diffused transmittance tomography

Nic An tSaoir, M., McMaster, M., Hardacre, C., Aiouache, F., Fernandes, D. L. A., Sá, J., & Kitagawa, K. (2011). Visualization of water vapour flow in a packed bed adsorber by near-infrared diffused transmittance tomography. *Chemical Engineering Science*, 66(24), 6407-6423. DOI: 10.1016/j.ces.2011.08.049

Published in:
Chemical Engineering Science

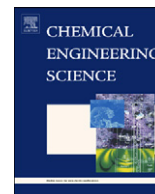
Queen's University Belfast - Research Portal:
[Link to publication record in Queen's University Belfast Research Portal](#)

General rights

Copyright for the publications made accessible via the Queen's University Belfast Research Portal is retained by the author(s) and / or other copyright owners and it is a condition of accessing these publications that users recognise and abide by the legal requirements associated with these rights.

Take down policy

The Research Portal is Queen's institutional repository that provides access to Queen's research output. Every effort has been made to ensure that content in the Research Portal does not infringe any person's rights, or applicable UK laws. If you discover content in the Research Portal that you believe breaches copyright or violates any law, please contact openaccess@qub.ac.uk.



Visualization of water vapour flow in a packed bed adsorber by near-infrared diffused transmittance tomography

Méabh Nic An tSaoir^a, Daniel Luis Abreu Fernandes^b, Jacinto Sá^c, Michael McMaster^a, Kuniyuki Kitagawa^d, Christopher Hardacre^a, Farid Aiouache^{a,*}

^a Queen's University Belfast, School of Chemistry and Chemical Engineering, Stranmillis Road, Belfast BT9 5AG, Northern Ireland, United Kingdom

^b Department of Chemistry, University of Aveiro, Campus de Santiago, 3810-193 Aveiro, Portugal

^c ETH Zürich, Chemistry and Bioengineering, Wolfgang-Paulistrasse 10, 8093 Zürich, Switzerland

^d Ecotopia Science Institute, Nagoya University, Chikusa-ku 464-8603 Nagoya, Japan

ARTICLE INFO

Article history:

Received 30 September 2010

Received in revised form

12 July 2011

Accepted 30 August 2011

Available online 9 September 2011

Keywords:

Near-infrared tomography

Visualization

Adsorption

Packed bed

Porous media

Transport processes

ABSTRACT

This work presents a procedure based on spatially-resolved near-infrared imaging, in order to observe temperature and composition maps in gas–solid packed beds subjected to effects of aspect ratio and non-isothermal conditions. The technique was applied to the water vapour flow in a packed bed adsorber of low aspect ratio, filled with silica gel, using a tuneable diode laser, focal planar array detector and tomographic reconstruction. The 2D projected images from parallel scanning permitted data to be retrieved from the packing and above the packing sections of $12.0 \times 12.0 \times 18.2 \text{ mm}^3$ at a volume-resolution of $0.15 \times 0.15 \times 0.026 \text{ mm}^3$ and a time-resolution of less than 3 min. The technique revealed uneven temperature and composition maps in the core packed bed and in the vicinity of the wall due to flow maldistribution. In addition, the heat uptake from the packed bed and local cross-mixing were experimentally ascertained by local profiles of the water vapour composition and temperature under various aspect ratios and feed flow rates. The relative deviations in temperature and compositions were 11.1% and 9.3%, respectively. The deviation in composition, which covers the packing and above the packing sections, was slightly higher than the deviation of 8% obtained up-to-date but was limited to the exit of a packed bed adsorber.

Crown Copyright © 2011 Published by Elsevier Ltd. All rights reserved.

1. Introduction

Until recently, gas–solid processes were examined using ‘single point’ spectroscopic techniques. These techniques have aided the understanding of fundamental phenomena using simplified concepts relying on pseudo-homogeneous descriptions of underlying events, which are often not valid at different spatial scales and use averaged concentration, temperature and packing structure data (Urakawa and Baiker, 2009; Weckhuysen, 2009). Previous work by our group on fluid flow and chemical kinetics in monolith reactors using spatial mass spectroscopy (SpaciMS) has demonstrated that local flow fields have a significant impact on the concentration, temperature and pressure drop distributions, thereby leading to oscillating concentrations, changes in temperature and partial breakthrough during carbon monoxide (CO) oxidation (Sa et al., 2010). However, the SpaciMS technique is an intrusive technique due to the need to insert a capillary inside the monolith reactor in order to analyse the gas composition. Even with capillaries of the order of $150 \mu\text{m}$, an increase

of 5% in the gas flow velocity and an increase of 19% in the pressure drop across the monolith were observed. Non-intrusive methods that provide a solution to this issue and these techniques, including spatially-resolved spectroscopy techniques, have gained in popularity over the last decade. These approaches have revealed that the averaged information commonly obtained concerning the performance of gas–solid processes in terms of activity, selectivity and stability, are in fact the consequence of a complex interplay between different physico-chemical gradients of concentration, temperature and velocity across different length scales (Weckhuysen, 2009). A well-known example is the catalytic oxidation of carbon monoxide (CO) on a Pt/Al₂O₃ catalyst. Spatiotemporal oscillation patterns and moving fronts originating from the segregated diffusion of CO were observed by infrared thermography at a spatial resolution of millimetres, while spiral waves on an enhanced defect density of Pt surfaces were revealed by two-dimensional (2D) photoemission electron microscopy at a spatial resolution of nanometres (Lindstrom and Tsotsis, 1986). Further examples have been cited in recent reviews on spatiotemporal techniques and catalysis by Urakawa and Baiker (2009) and Weckhuysen (2009).

Packed beds of gas–solid systems are extensively used as reactors, separators, dryers, filters and heat exchangers. The design of packed

* Corresponding author.

E-mail address: f.aiouache@qub.ac.uk (F. Aiouache).

beds requires an extensive knowledge of local dynamics of compositions and temperature leading to numerous investigations over the past few decades (Magnico, 2009; Nijemeisland and Dixon, 2004). Unfortunately, most of this research was dedicated towards the development of computer fluid dynamics codes whereas little advances were achieved on the experimental procedures. In general, three-dimensional distributions of temperature and composition in gas–solid systems are simulated with little difficulty nowadays, but the experimental measurement is not sufficiently mature. Dispersion profiles, which show the effectiveness of heat and mass transfers inside and around the solid beads of a packed bed, are commonly measured by multiple experiments in which invasive probes are placed at different locations, leading to different residence time distributions (Coppens, 2005; Nijemeisland et al., 2004; Nijemeisland and Dixon, 2004; Freund et al., 2005). However, recent developments in spatially-resolved techniques have allowed magnetic resonance imaging (MRI) (Rigby and Gladden, 1996), X-ray (Roels and Carmeliet, 2006) neutron (Asano et al., 2005) and laser spectroscopy (Cai et al., 2009) to measure anisotropic dispersion profiles in gas–solid and liquid–solid reactors, achieving rapid access to scalar data of chemical kinetics and associated mass transfers in a single experiment. These techniques allow three-dimensional (3D) distributions along axial, radial and circumferential directions of the bed structure, such as porosity, pore size and tortuosity, to be mapped within the macroscopic (0.01–10 mm) heterogeneity of the packing. Unfortunately, these techniques have not been adaptable or sufficiently mature to be applied to a wide spectrum of gases in gas–solid processes, due to the inherently weak signals from the gaseous phase. Nevertheless, optical techniques are increasingly cited in both the open and industrial literature, being chemical species sensitive and eventually boosted by rapid developments in tuneable lasers and single or 2D array detectors, leading to experiments being performed at high spatiotemporal resolutions. Nadeau et al. (1996) measured a residence time distribution in the order of milliseconds, by directing an infrared laser light at different locations of a reactor using methane as a tracer probe. The sub-second response time resolution allowed rapid observation of local maldistribution and radial dispersions. Hindle et al. (2001) used optical tomography to observe the spatial distributions of hydrocarbons at the exit of a combustion chamber; Reinke et al. (2005) coupled Raman and laser-induced fluorescence techniques to observe the spatial distribution of stable and radical species between two catalytic plates accessible by lateral transparent windows, during the catalytic partial oxidation of methane. Salem et al. (2005) used near-infrared (NIR) transmittance tomography to observe the spatial breakthrough of water vapour in a packed bed adsorber. This technique relied on an NIR light from a distributed feedback diode laser that was split into three lights, collimated to the exit of a packed bed adsorber, and detected by three InGaAs photodiode arrays. The wall effect on adsorption breakthrough was demonstrated in a packed bed adsorber with a low aspect ratio of tube to particle diameters. All these works however used optical tomography at the exit of the packed beds to circumvent light deflection and scattering across the packed beds.

NIR diffused transmittance tomography (NIRDTT) is less energetic than MRI tomography, X-ray tomography or neutron tomography, but recent advances in this technique have led to its increased usage for biomedical applications such as quantifying organ function (Arridge et al., 2000). The transport of NIR light in a scattering environment such as biomaterials is nearly isotropic and is consequently well-predicted by photon diffusion models. NIRDTT presents several advantages simply because it uses affordable instrumentation (BK7 optics, quartz-based equipment and diode lasers), traverses greater depths in scattering environments and is relatively less attenuated by fluids compared with infrared, which in turn lead to the technique being applicable for

gas flow observations (Carey et al., 2000). NIRDTT has been widely used in low scattering media such as combustion imaging where simultaneous measurements of concentration and temperature of gases by absorption spectroscopy and by the so-called ‘two-line thermometry’, respectively, were recorded (Terzija et al., 2008). Two-line thermometry uses the ratio of absorbance of two line transitions originating from lower states with dissimilar absorption energies. Water vapour is often used as a tracer owing to its strong absorption lines of the combination bands in the near-infrared (Ma et al., 2009).

In the present work, an experimental procedure based on spatially-resolved NIR imaging is presented. The technique’s capability has been demonstrated by observing water vapour flow in a packed bed adsorber with a low aspect ratio of tube to particle diameters (D_t/d_p) where the flow is subject to entrance effects, wall effects and non-isothermal conditions. This design may correspond to the control of drying of a carrier gas containing moisture in purification processes but also the deactivation of catalyst by water vapour in gas–solid reactions for example in the oxidation of carbon monoxide (Son, 2003), decomposition of ozone (Yang et al., 2006), low temperature water–gas-shift (Goguet et al., 2007) and Fischer–Tropsch (Tsakoumis et al., 2010). It is well known that packed beds of low aspect ratios exhibit wall effects on the flow due to variable radial porosity. For low aspect ratios, particularly for values of ten or less, there is an additional influence of the confining walls, which creates regions of high porosities in the vicinity of a wall. Intensive properties, such as density, concentration and velocity, therefore, follow the same trend as the porosity due to fluid continuity, leading to maldistribution and discrepancy from the uniform flow. Unlike aforementioned optical tomography techniques, which were adapted to the exit of the packed beds, in this work, NIRDTT retrieved from the interior of the packed bed and the non-linearity effects were reduced by a dedicated experimental design and an image reconstruction procedure. The main design used to observe the flow spatial heterogeneity by NIRDTT employs a tuneable diode laser, focal planar array (FPA) detector and tomographic reconstruction. Silica gel of low light scattering effect is used as the packing and adsorbing material. This procedure takes advantage of the rapid developments in fibre optics and high-speed electronics of FPA detectors leading to a time resolution of a full packed tomography in a few minutes. The effects of the aspect ratio and feed flow rate on the composition and temperature fields, and the consequences for the associated transports, are discussed.

2. Material and methods

An NIR tomography set-up was designed by collecting data from line-of-sight 2D visualization of the full packed bed. 3D distributions of temperature and composition in and above the packing were obtained simultaneously. The adsorption set-up is shown in Fig. 1. The tube was made of fused quartz of 9 mm I.D. and was filled with 0.75 g of silica gel. Silica gel (Davicat[®] SI 1102 average pore diameter 14.4 nm, pore volume 1.12 cm³ g⁻¹, BET surface area 331 m² g⁻¹) had been treated with a solution of dimethyldichlorosilane to form a silicone layer around the silica and thus reduce its highly hydrophilic character. Typically, water vapour was introduced to the system from a controlled evaporator mixer (Bronkhorst) at a flow rate of 338 cm³ min⁻¹ of N₂, a water composition of 6.0 mol% (relative humidity of 30.5%) and temperature of 333 K, with all pre- and post-packed tube pipes being insulated and heated to the operating temperature. Thermocouples were placed before and after the packed bed, to validate the feed temperatures obtained by NIRDTT. In addition, a humidity sensor (Exo Terra Digital Hygrometer, accuracy 2%

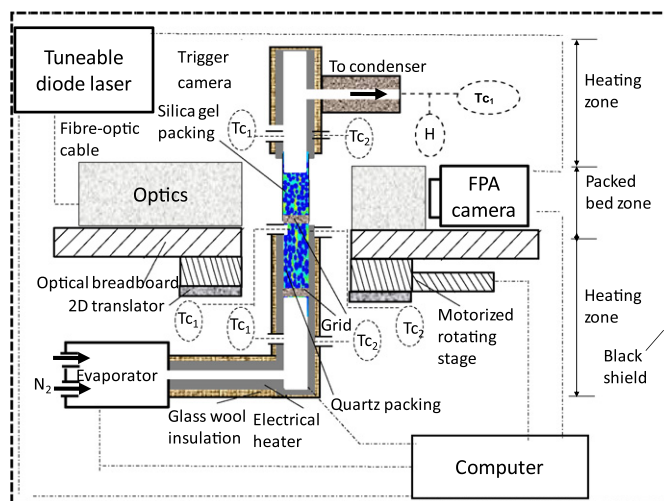


Fig. 1. Scheme of the whole tomography apparatus: Evaporator (Bronkhorst)=Mass flow controller (N_2), air-actuated switching valve, distilled water bath; H: Humidity sensor; TC_1 =Thermocouples (monitoring), TC_2 : Thermocouples connected to programmable temperature controllers; Optics=details of optics are shown in Fig. 3; Tuneable diode laser: Lock-in monomode connected to FPA camera; Quartz packing: pre-packed bed mixer, Silica gel packed bed=Height:14 cm; visible aperture by NIR camera: $1.20 \times 1.82 \text{ cm}^2$.

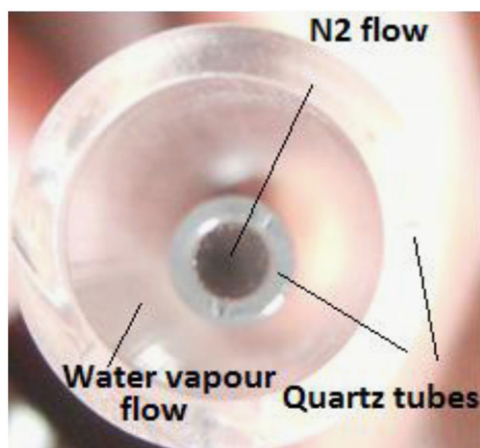


Fig. 2. Quartz cell for validation tests. Inner tube diameter: 5 mm, quartz cell diameter: 9 mm, thickness of both tubes: 0.5 mm.

at relative humidity $> 10\%$) was placed at the exit of the experimental set-up as shown in Fig. 1, where temperatures were lower than the operating ones, leading to compositions down to 1.0 mol% to be validated. The entire experimental set-up was enclosed within a black-shielded Perspex box and purged of excess moisture by dry nitrogen.

Validation of the 3D imaging of the water vapour composition and temperature was carried out using a quartz cell of 9 mm I.D., filled with silica gel and inserted by an empty quartz tube of 5 mm I.D. in the centre of the cell as shown in Fig. 2 and detailed in Section 4.1. Water vapour was blown into the quartz cell and N_2 was injected through the inner tube, providing the near-wall region and the central core region with flow mixtures rich in water vapour and N_2 , respectively.

The tomography technique relied on the principle of the recent generation of tomographs, which rely on 2D projected images from parallel scanning as shown in Fig. 3. An NIR laser source and an FPA NIR detector were coupled so that the detector was always facing the source. They were then rotated linearly to acquire a single projection, which measured both the transmission data through the water

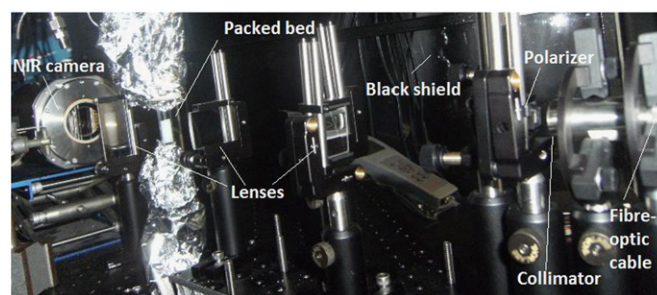


Fig. 3. Photograph of optical set-up (laser source not visible).

vapour medium and the diffused transmission data through the packed bed. Acting as a light source, a continuous wavelength tuneable diode laser (Santec TSL-510) with a line width of 1 MHz, a modulating range from 1340 to 1440 nm, scanning speed of 100 nm s^{-1} and an output power of 4 mW was tuned to the high-absorption frequencies of water vapour. The laser beam was polarized before being collimated by a series of mirrors and cylindrical lenses in order to shape a top-hat and rectangular sheet beam of $12.0 \times 18.2 \text{ mm}^2$ size as shown in Fig. 4. This laser sheet beam trans-illuminated both the packing section and the empty section above the packing and was then collected by an image-intensifying low light FPA detector (Mosir 950 detector, Intervac, 1024×256 pixels, $26 \times 26 \mu\text{m}^2/\text{pixel}$) at 2 MHz and 15 scans/test, recorded as a 16 bit grey-scale image, and processed by the image processing software VSpecPro (Intervac). Motion control of the optical stage was achieved by the use of a servo-motor, which allowed 3D translation and rotation around the central axis of the packed cylinder.

3. Results and discussions

The applicability of NIRDTT to water vapour flow in packed beds is demonstrated by the three following sections: (a) the procedures for temperature and composition measurements and tomographic reconstruction; (b) the validation tests and (c) the application to water vapour flow in a packed bed adsorber of low aspect ratio, where the effects of the aspect ratio, the non-isothermal conditions and the flow dynamics are discussed.

3.1. Temperature and composition measurements

3.1.1. Composition measurement

The composition of the water vapour was calculated by assuming that the brightness of a visualized image is proportional to the laser light intensity I_λ that trans-illuminates the packed bed and is intercepted by the NIR detector as expressed

$$I_\lambda(x,y) = G \exp\left(-\varepsilon_\lambda \int C dl\right) + O_\lambda(x,y) \quad (1)$$

where G is the gain of the NIR detector, ε is the absorption coefficient, l is the optical path length, C is the uneven composition of water vapour across the packing and $O_\lambda(x,y)$ is the offset value in brightness intensity, which was caused by the packed bed particles, adsorbed phase of water vapour on the silica gel and the dark current of the NIR detector. Assuming that the offset value was weakly dependent on the changes of attenuation wavelength, Eq. (1) reduces to Beer's law:

$$\text{Abs}(T,\lambda) = -\log_{10} \frac{I_{\lambda 2}}{I_{\lambda 1}} = \varepsilon(T,\lambda) \int C dl \quad (2)$$

where Abs is the integral absorbance and $I_{\lambda 2}$ and $I_{\lambda 1}$ are the NIR intensities at high and low absorption wavelengths of water

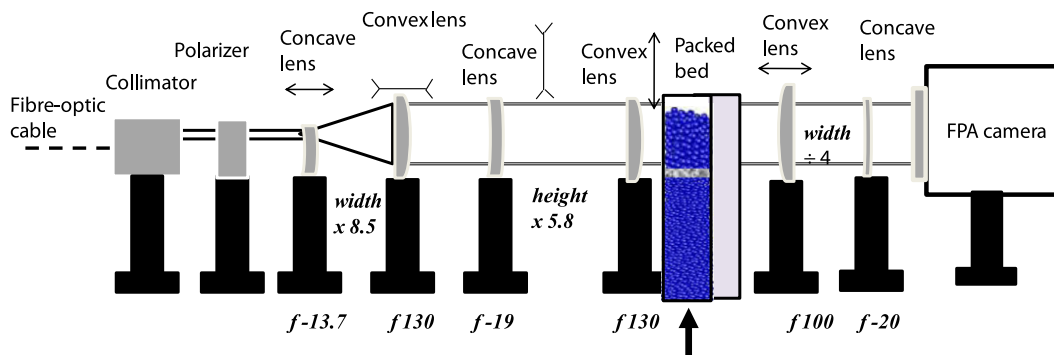


Fig. 4. Monomode fibre-optic cable connected to a collimator with a top-hat beam shaper (size: 5 mm); polarizer, two couple of cylindrical lenses of focal points f (mm): f -13.7, f -130 and f -19, f -130, trans-illuminated backed bed and couple of lens (f -100, f -20) and intercepted beam size by FPA detector (12.0×18.2 mm).

Table 1

Absorption coefficient profiles with temperature at 1380.685 nm in both packing phase and vapour phase above the packing phase.

| Wavelength (nm) | $\varepsilon_{\text{Packing phase}} (\text{m}^{-1}\text{atm}^{-1})$ | $\varepsilon_{\text{Vapour phase}} (\text{m}^{-1}\text{atm}^{-1})$ |
|-----------------|---------------------------------------------------------------------|--------------------------------------------------------------------|
| 1380.685 | $-7 \times 10^{-6}T^3 + 0.0071T^2 + 2.458T - 281.25$ | $-3 \times 10^{-5}T^3 + 0.0277T^2 - 9.6013T + 1138.6$ |

vapour, respectively, which correspond to the actual water vapour composition.

The absorption coefficients of H_2O across the solid packing and the empty section above the packing were obtained experimentally using a squared quartz cell, which was half-filled with the packing. The absorption coefficients were measured at a wavelength of 1380.685 nm and a temperature ranging from 323 to 363 K. The measured absorption coefficients were fitted to a polynomial model as a function of temperature. The selection of the wavelength 1380.685 nm was because of the sensitivity of its corresponding absorption line to temperature, as shown in Section 3.1.2. Table 1 reports the absorption coefficient profiles with temperatures for the packing phase and gaseous phase above the packing. In the packing medium, the optical depth provided an approximation to the average extinction coefficient during the passage of light through the packing medium. The average optical depth through the packing without water vapour of 0.3 led to a scattering number of less than unity and to a straight propagation of the NIR light with a negligible scattering through the packing. When water vapour was added, an averaged ratio of absorbance through the packing and above the packing at 1380.685 nm and temperature 333 K was 0.48 offering an effective path through the packing of 30% higher than the path above the packing.

3.1.2. Temperature measurements by two-line thermometry

The water vapour temperature was measured by computing the ratio, R , of the integral absorbances Abs_1 and Abs_2 for two temperature-dependent transitions (Zhou et al., 2003):

$$R = \frac{Abs_1(T, \lambda_1)}{Abs_2(T, \lambda_2)} \quad (3)$$

The two integral absorbances were taken from the same interrogatory area in terms of composition and path length. The integral absorbance ratios, R , could then be simplified to absorption coefficient ratios:

$$R = \frac{\varepsilon_1(T, \lambda_1)}{\varepsilon_2(T, \lambda_2)} \quad (4)$$

where the absorption coefficient ε_i is the product of the line strength, $S(T)$, of the temperature-dependent transition and line

shape function, $\varphi(\lambda)$, as illustrated by Eq. (5) (Zhou et al., 2003). The latter was approximated to unity after normalization ($\int \varphi(\lambda) d\lambda = 1$) (Shao et al., 2009):

$$\varepsilon_i = S_i(T, \lambda_i) \varphi_i = S_i(T, \lambda_i) \quad (5)$$

The integral absorption ratio, R , in turn was approximated to the line strength absorbance ratio, as shown by

$$R = \frac{S_1(T, \lambda_1)}{S_2(T, \lambda_2)} \quad (6)$$

where the line strength at an arbitrary temperature T is related to a reference temperature T_0 as shown by (Zhou et al., 2003):

$$S_i(T) = S_i(T_0) \frac{Q_i(T_0)}{Q_i(T)} \left(\frac{T_0}{T} \right) \exp \left[-\frac{hcE_i}{k} \left(\frac{1}{T} - \frac{1}{T_0} \right) \right] \frac{[1 - \exp(-hc/kT\lambda_0)]}{[1 - \exp(-hc/kT_0\lambda_0)]} \quad (7)$$

where $Q_i(T)$ is the temperature-dependent partition function of the water vapour, $S_i(T_0, \lambda_i)$ is the line strength of the transition centred at line wavelength λ_i for a reference temperature T_0 , often taken at 296 K; h is Planck's constant; c is the speed of light; k is Boltzmann's constant; E_i is the lower state energy and T is the gas temperature (K). The integral absorbance ratio is thus related to the temperature by

$$R = \frac{S_1(T_0)}{S_2(T_0)} \exp \left[-\frac{hc(E_1 - E_2)}{k} \left(\frac{1}{T} - \frac{1}{T_0} \right) \right] \frac{[1 - \exp(-hc/kT\lambda_1)]}{[1 - \exp(-hc/kT\lambda_2)]} \quad (8)$$

The selection of line pairs was, however, not trivial. The widespread and strong absorption transitions provided many options for measuring H_2O and temperature. Criteria set by Zhou et al. (2003) recommend lines to be strong, not overlapped and have dissimilar temperature dependences. Based on this criteria and the fact that the employed laser limited the wavelength range to 1340–1440 nm, the search for a suitable candidate pair of lines in the $\nu_1 + \nu_3$ combination band, using the database (Rothman et al., 2009), resulted in a pair of lines at 1358.412 and 1380.685 nm being selected as shown in Fig. 5. These lines were found to be a good fit in terms of temperature sensitivity, since they offer a difference in lower state energy ($E_2 - E_1$) of 283 cm^{-1} , a line strength ratio at reference temperature ($S_1(T_0)/S_2(T_0)$) of 1.19 and are close but do not overlap. Fig. 5(a) shows experimental spectra through the packing and above the packing in the vicinity of the

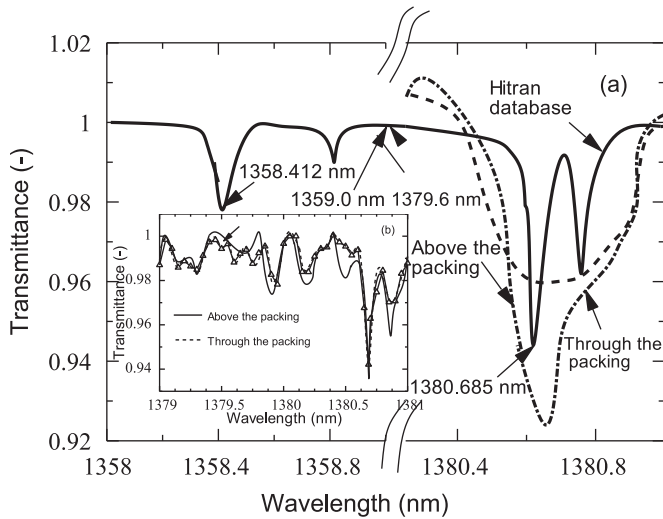


Fig. 5. Simulated and experimental transmittance spectra of water vapour lines. Temperature= 333 K, pressure= 1.013×10^5 Pa, optical path= 10^{-2} m, composition of H_2O in $N_2=6$ mol%.

transition line of 1380.685 nm and Fig. 5(b) shows the maximum change in the background noise with respect to the transition lines in the vicinity of 1380.685 nm. The maximum noise in terms of transmittance reached a value about 0.98 as shown in Fig. 5(b). Apart from the transmittance, the two spectra of transmittance through the packed bed and above the packed bed show no difference in terms of the background noise and peak shape profiles suggesting a similar path of propagation of the light through and above the packing. An averaged deviation between the transmittance spectra at 1380.685 nm and temperature of 333 K, which were obtained above packing in Fig. 5(a) and the one retrieved from Hitran database (Rothmans et al., 2009) was 2.5%.

3.2. Data processing and tomographic reconstruction

The tomographic reconstruction was performed using an iterative method, a so-called ‘adaptive algebraic reconstruction technique’ (AART) (Dyakowski and Jaworski, 2003), which was written in MATLAB code and designed for the purpose of simultaneous measurements of temperature and composition. AART reconstructed on a discretized domain a 3D object function, $f(x,y,z)$, of unit coordinates (i,j,k) , which was either local temperature or composition. Although significantly slower than well-known analytical methods based on the inverse Radon transform and filtered backprojection, AART offers more flexibility in terms of limited data sets of projections and a reasonable compromise between convergence rate and accuracy, while being more tolerant to noisy data. The object function was modelled as an array of discrete unknown voxels or cells, leading to a system of equations. This array of unknown voxels resulted from a parallelepiped grid, which was superimposed on the function $f(x,y,z)$ and had dimension $m \times m \times N$, providing a total number of voxels: $M=N \times m^2$ as reported in Fig. 6. Each voxel was given a single index representation with the numbering sequence starting in the upper left-hand corner of the parallelepiped voxel array. Within each voxel, the function $f(x,y,z)$ was assumed to be constant with a value of the voxel, located at the k th and j th pixels, designated f_{kj} . For the i th hyperplane ray, p_i was the measured value of the experimental integral absorbance Abs for

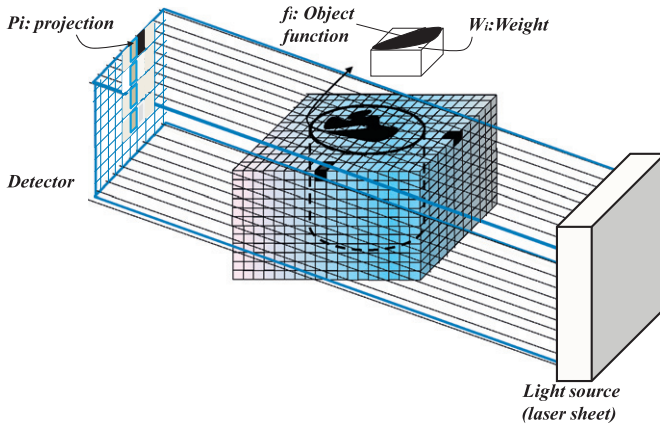


Fig. 6. Image reconstruction using parallel beam and voxel division.

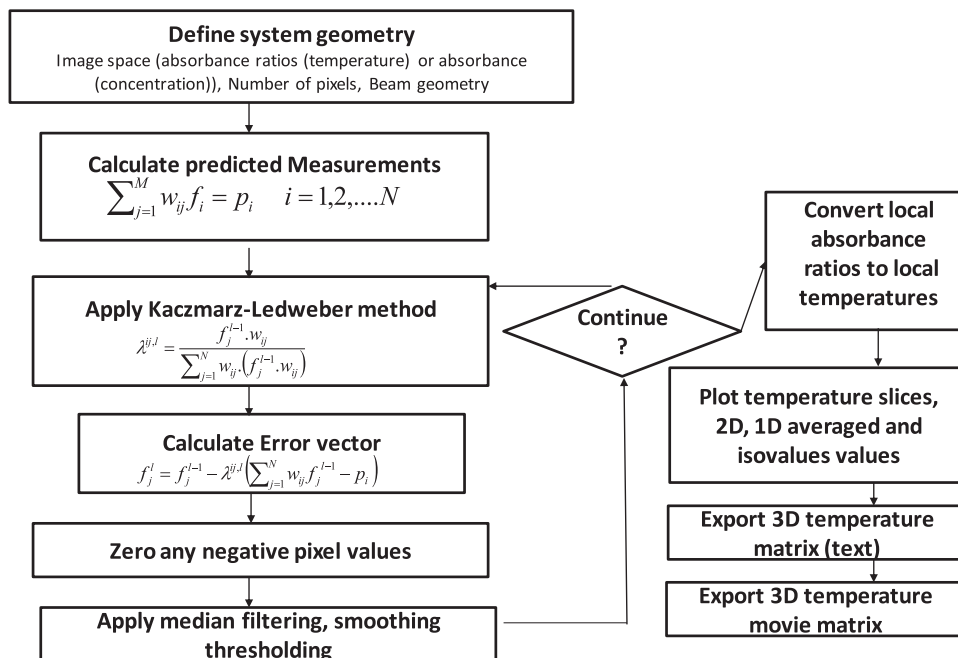


Fig. 7. Image reconstruction algorithm of adaptive algebraic reconstruction method for local temperature. Local composition reconstruction (composition slices, 2D averaged values, 1D averaged values, iso-values, composition matrix (text) and 3D composition in a movie matrix) used the same algorithm where local absorbance ratios were replaced by local absorbance.

composition measurements or integral absorbance ratio R for temperature measurements along the path as expressed by Eqs. (2) and (8), respectively.

The algorithm, as shown by Fig. 7, started by setting an initial arbitrary estimate for the voxel vector and then projecting onto the first hyperplane equation. The resulting point was projected

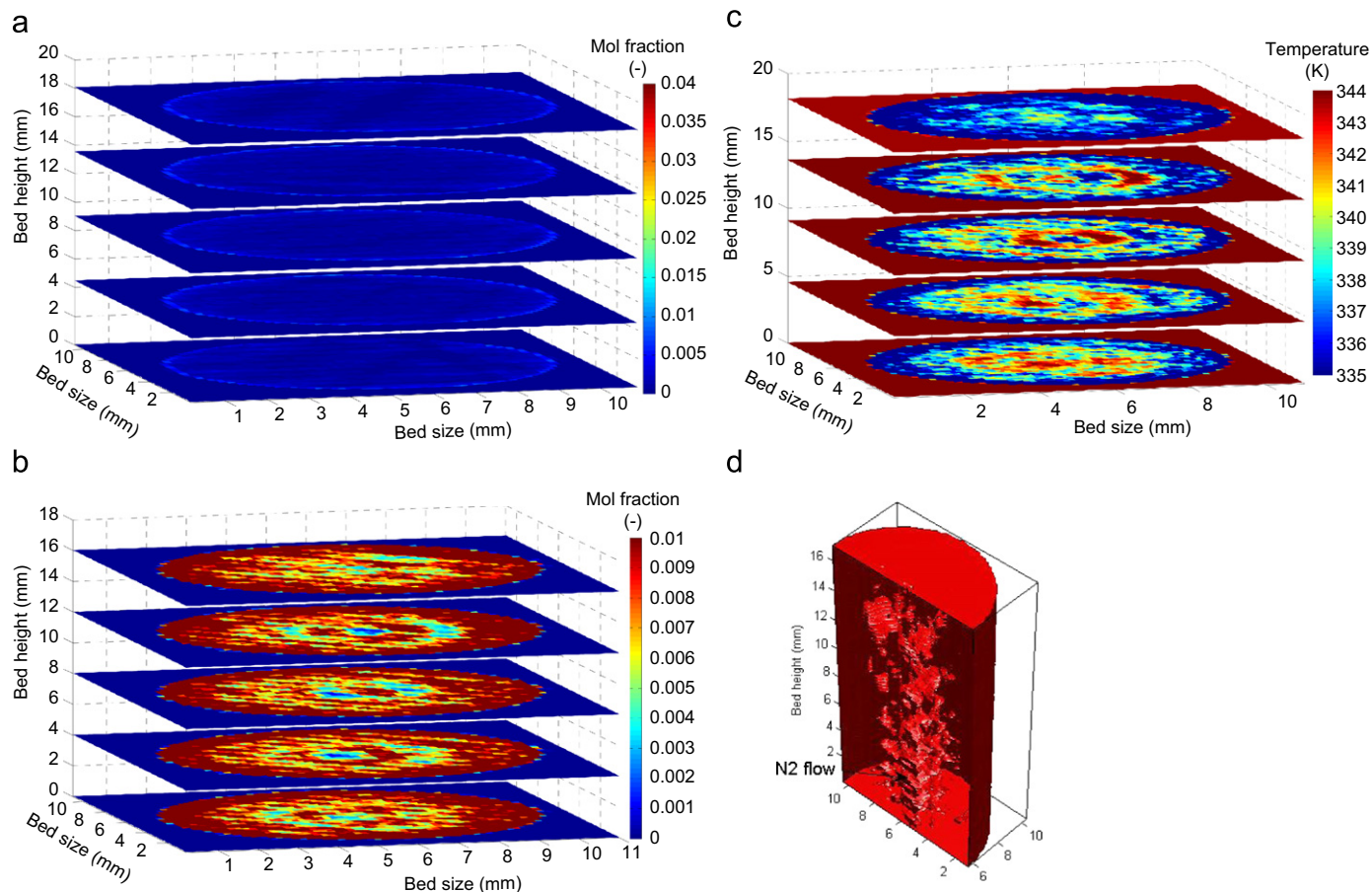


Fig. 8. Visualization of water vapour flow exit of two-concentric quartz (a) N_2 flow (b) equidistant cross-sectional composition maps from N_2 exit section from the inner tube and (c) equidistant cross-sectional temperature maps from N_2 exit section from the inner tube and (d) 3D water vapour composition at an iso-value mole fraction of 0.01, bed height: 14 mm, particle size: 0.7 mm (AR: 13), wall temperature: 333 K, water vapour composition: 6.0 mol%, N_2 velocity: 0.086 m s^{-1} , water vapour velocity: 0.086 m s^{-1} .

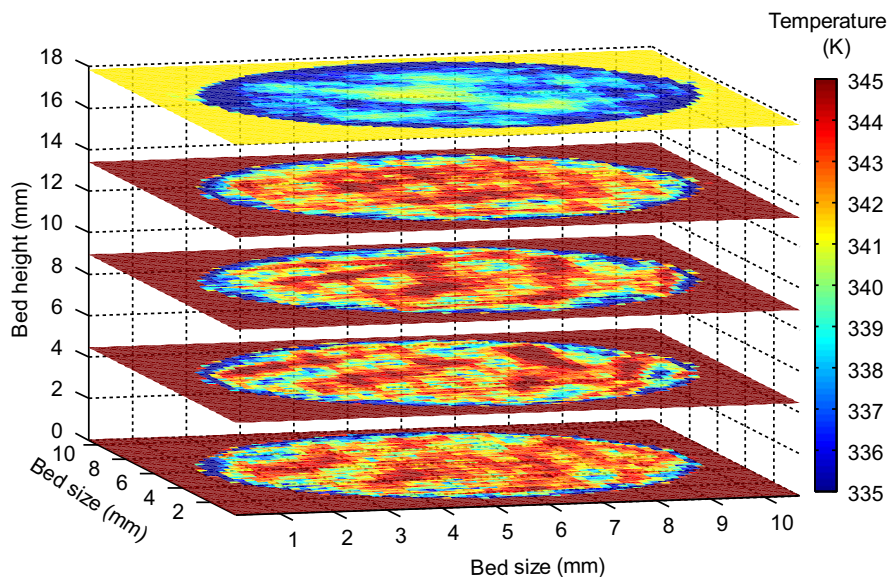


Fig. 9. Transient temperature maps of five cross-sectional layers located at equal distance from the bottom of the packing to the top of the vapour phase above the packing, time: 60 min, packing height: 14 mm, particle size: 0.7 mm (AR: 13), wall temperature: 333 K, water vapour composition: 6.0 mol%, N_2 flow rate: $338 \text{ cm}^3 \text{ min}^{-1}$.

onto the next hyperplane equation, and so on until the final hyperplane equation. The system of hyperplane algebraic equations is written as follows:

$$\sum_{j=1}^M w_{ij} f_j^l = p_i, \quad i = 1, 2, \dots, N \quad (9)$$

where w_{ij} is the weighting factor representing the contribution of the j th cell to the i th measurement, N is the total number of projection rays and M is the total number of voxels. The numerical value of the weighting factor w_{ij} is equal to Abs or R of the 3D image cell (k th, j th pixels) intercepted by the i th hyperplane ray. The Kaczmarz method was then used for solving algebraic equations

(Dyakowski and Jaworski, 2003). The iterative equation is

$$f_j^l = f_j^{l-1} - \lambda^{ij,l} \left(\sum_{j=1}^N w_{ij} f_j^{l-1} - p_i \right) \quad (10)$$

where $\lambda^{ij,l}$ is a relaxation parameter, which is defined by

$$\lambda^{ij,l} = \frac{f_j^{l-1} w_{ij}}{\sum_{j=1}^N w_{ij} (f_j^{l-1} w_{ij})} \quad (11)$$

Here, $f_j^{k-1} w_i$ is the dot product and k is the iteration index. Reconstruction of cross-sectional images or slice matrixes was repeated for each subsequent cross-sectional matrix until the 3D local absorbance ratios, R , for temperature reconstructions and the

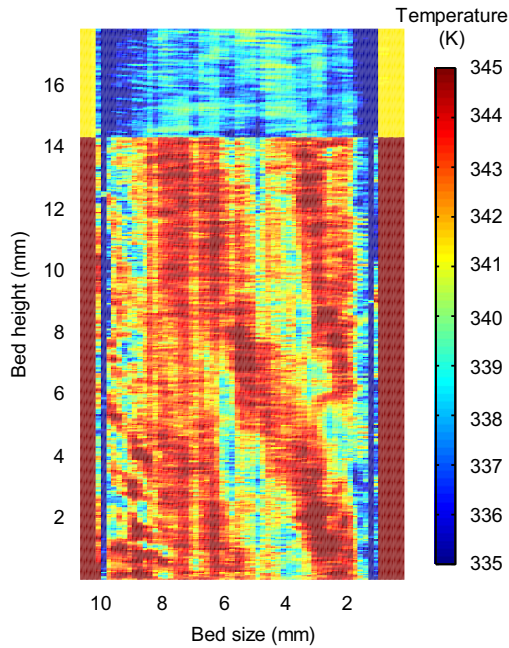


Fig. 10. Vertical cross-section of transient temperature distribution through the centre of the packed bed, time: 60 min, packing height: 14 mm, particle size: 0.7 mm (AR: 13), wall temperature: 333 K, water vapour composition: 6.0 mol%, N_2 flow rate: $338 \text{ cm}^3 \text{ min}^{-1}$.

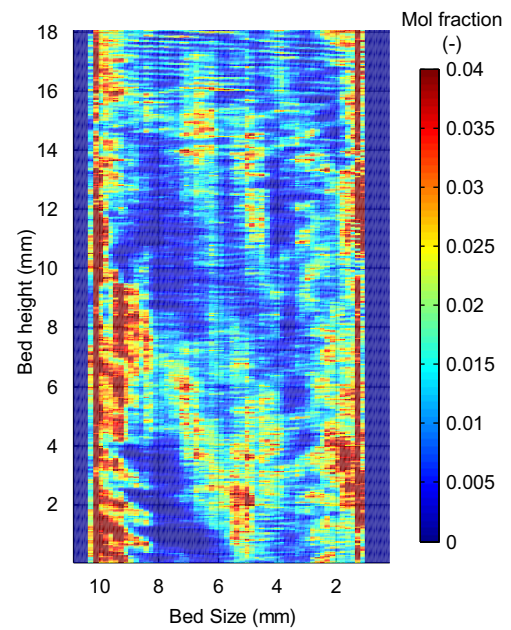


Fig. 12. Vertical cross-section of transient water vapour composition map through the centre of the packed bed, time: 60 min, packing height: 14 mm, particle size: 0.7 mm (AR: 13), wall temperature: 333 K, water vapour composition: 6.0 mol%, N_2 flow rate: $338 \text{ cm}^3 \text{ min}^{-1}$.

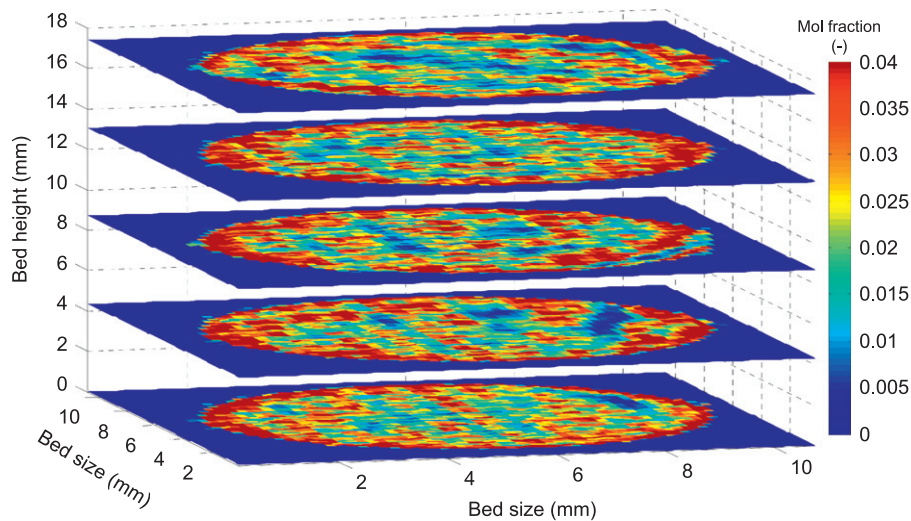


Fig. 11. Transient water vapour composition maps of five cross-sectional layers located at equal distance from the bottom of the packing to the top of the vapour phase above the packing, time: 60 min, packing height: 14 mm, particle size: 0.7 mm (AR: 13), wall temperature: 333 K, water vapour composition: 6.0 mol%, N_2 flow rate: $338 \text{ cm}^3 \text{ min}^{-1}$.

local absorbance, Abs , for composition reconstructions were obtained for the packing and the above packing regions of the packed cylinder. The local absorbance ratio and local absorbance were then further converted to temperature and composition using Eqs. (2) and (8), respectively. It should be noted that since the observed process was

not isothermal, the programme first calculated the temperatures above and within the fully packed bed, and then exported these temperatures as a 3D matrix. This matrix was used for measurements of the temperature-dependent absorption coefficients according to the correlations listed in Table 1, and these absorption

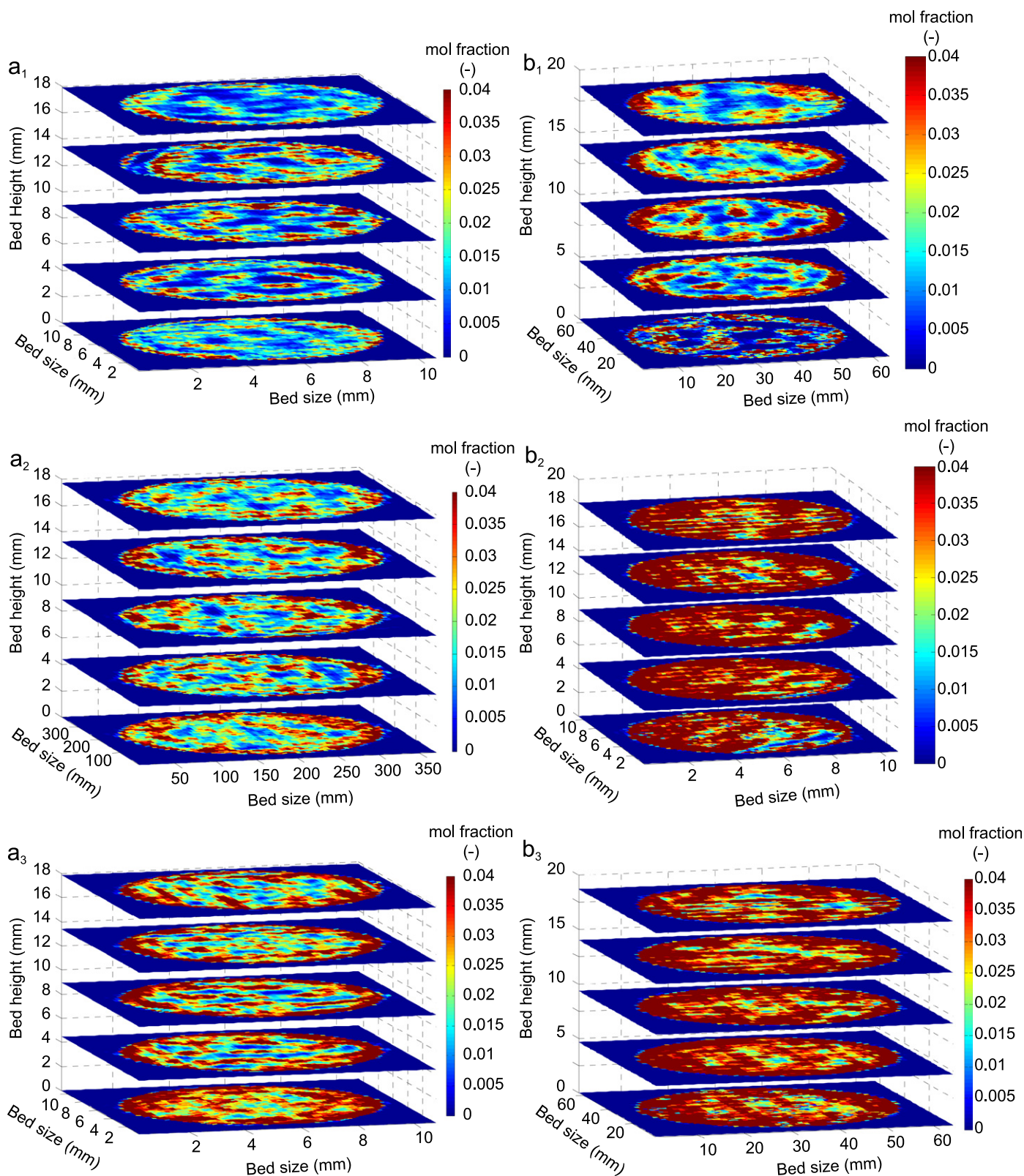


Fig. 13. Wall effect on transient water vapour distribution at three aspect ratios of 3 (a_1 – a_3), 9 (b_1 – b_3) and 13 (c_1 – c_3), subscripts 1, 2 and 3 correspond to 5, 60 and 240 min, respectively, packing height: 14 mm, wall temperature: 333 K, water vapour composition: 6.0 mol%, N_2 flow rate: $338 \text{ cm}^3 \text{ min}^{-1}$.

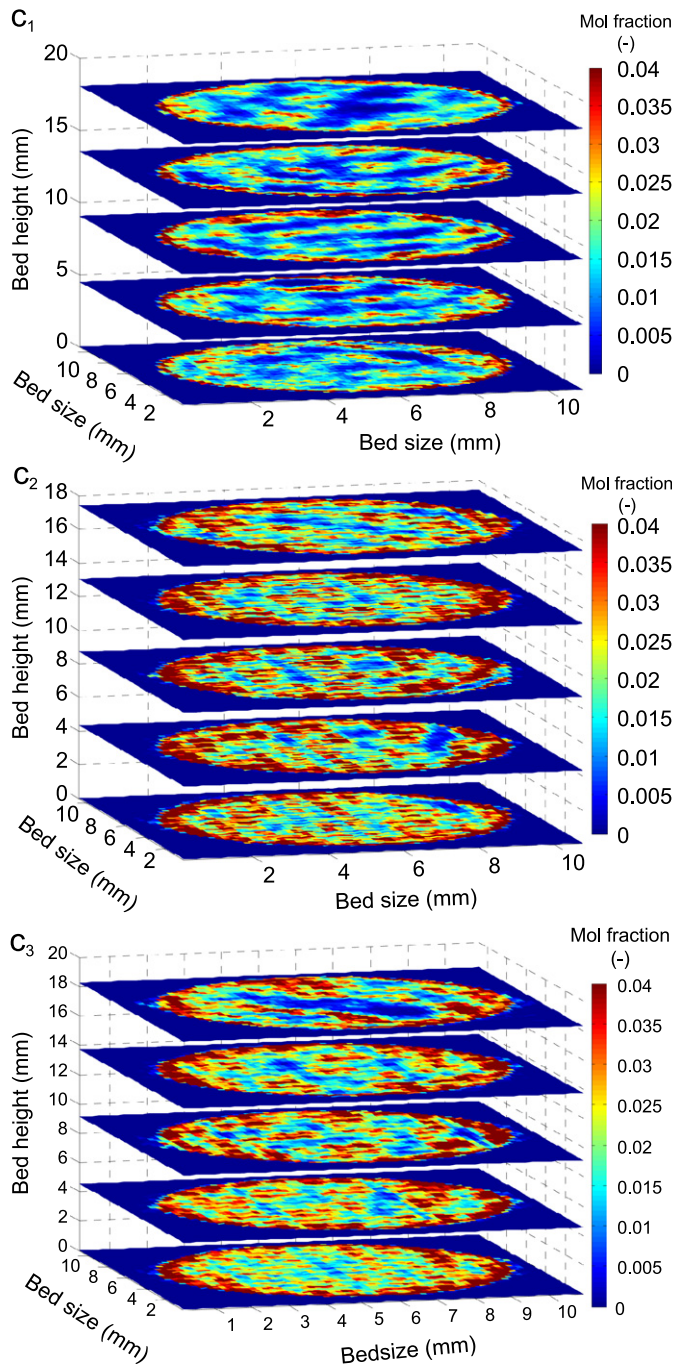


Fig. 13. (continued)

coefficients in turn were used for the tomographic reconstructions of the compositions.

4. Application to water vapour flow in a packed bed adsorber

4.1. Validation by 3D imaging of the mass and thermal dispersions of water vapour flow in a packed bed

The first validation test represents the steady-state flow of water vapour as a tracer inside the packed bed adsorber filled with silica gel particles while pure N_2 was injected into the centre of the cross-section by a tube of 5 mm I.D. as shown in Fig. 2. Both flows were at similar superficial velocity of 0.086 m s^{-1} .

The length of the packing section was 14 mm. 3D reconstructed images of water vapour composition and temperature were generated for the projections taken at fixed angle steps of 15° , one cycle of thirteen projections lasted approximately 3 min and a typical reconstruction required about 180 min on a 2.0 GHz computer. The maximum size of the pixel array of NIR detector that could collect the trans-illuminated NIR beam (size of $12.0 \times 18.2 \text{ mm}^2$) was 80×700 pixels, leading to a spatial resolution of $0.15 \times 0.026 \text{ mm}^2$. The accuracy in terms of composition and temperature of the water vapour distribution generated was investigated by varying the water vapour composition from 1 to 6 mol% and the temperature from 323 to 353 K. The original (reference) image is presented in Fig. 2 while the reconstruction images of the water vapour composition and temperature, before and after the introduction of water vapour at a composition of 1.0 mol% and a temperature of 333 K, are shown in Fig. 8(a) and (b)/(c), respectively. Fig. 8(b) and (c) shows five cross-sectional composition and temperature maps from the bottom to the top of the packed bed whereas Fig. 8(d) shows the 3D iso-values of water vapour composition at 1.0 mol%. A high composition of water vapour is well displayed in the vicinity of the wall (outer flow) and clear limits between the water vapour flow region and non water-flow region are easily discernible from the bottom slice (the exit of the inner tube) to the top slice (the end of the packed bed). In addition, the composition and temperature maps clearly discriminate water vapour maps and their respective temperature maps as shown by the blue zones in area rich in N_2 . These results were compared with results from a thermocouple and humidity sensor placed at the empty section above the packed bed. The cross-sectional averaged values of composition and temperature obtained by NIRDIT were 0.73 mol% and 342 K whereas the humidity sensor and thermocouple indicated 0.64 mol% and 336 K, respectively. The averaged relative deviations in water vapour composition and temperature for full ranges of 1 to 6 mol% and 323 to 353 K investigated were 11.1% and 9.3%, respectively.

4.2. Water vapour flow in a packed bed adsorber of low aspect ratio (Dt/dp)

Reconstruction of 3D images of water vapour in regions close to the wall and respective temperature fields in a packed bed adsorber of low aspect ratio of tube to particle diameters (Dt/dp) was the second application of NIRDIT. The test was performed on a packed bed of an aspect ratio (AR) of 13, i.e., particle size of 0.7 mm, inlet and wall temperatures of 333 K and flow rate of $338 \text{ cm}^3 \text{ min}^{-1}$, to assess the changes of temperature and composition distributions with time in the packing and above the packing of the packed bed. The maldistribution of the flow was further assessed by varying the aspect ratio at conditions with and without transport limitations, i.e., particle size and feed vapour flow rate.

4.2.1. Transient temperature and composition profiles during adsorption dynamics

4.2.1.1. Temperature profiles. Fig. 9 shows temperature maps following 60 min of adsorption of five selected cross-sectional layers located at equal distances from the bottom of the packing to the top of the vapour phase above the packing where the four bottom layers belong to the packing section and the top layer to the empty section above the packed bed. The entire cross-sectional layers from the bottom to the top of the packed bed, which correspond to 700 layers, were gathered in a movie at a frame rate of 24 layers s^{-1} as shown in the supplementary material (S_1). Hot and cold zones with changes in temperatures up to 10 K are visible throughout the packing and the empty space above the packing. In the packed bed, two distinguishable

blue and red colour zones can be seen. The first zone is closer to the wall where convective heat transfer dominates due to the large porosity in contact with the wall. The second zone is the packing area, which starts from the silica particles, which miss contact with the wall, to the centre of the packing where heat transfer by conduction and convection occur, leading to efficient cross-mixing of the water vapour flow. It can be seen that the averaged wall temperature from the bottom to the top of the packed bed was 336 K while the averaged inlet temperature of the feed was 341 K. The effectiveness of wall cooling of the packed bed can, therefore, be qualitatively assessed by observing actual maps of the wall, of the

vicinity of the wall and central packing temperatures. Uneven temperature profiles are observed along radial and circumferential (angular) directions. Large drops in the temperature in the area near the wall and small changes in the temperature in the area towards the centre demonstrate inefficient heat transfer from the packing to the wall. Hot zones, therefore, correspond to the situation where the flow velocity was uniform along the axial and radial directions, while cold zones reflect a minimal flow velocity, resulting in a reduced energy transfer from the packing to the wall. In addition, an inefficient energy uptake is followed in some areas by a decrease in the temperature when moving towards the centre of the packing,

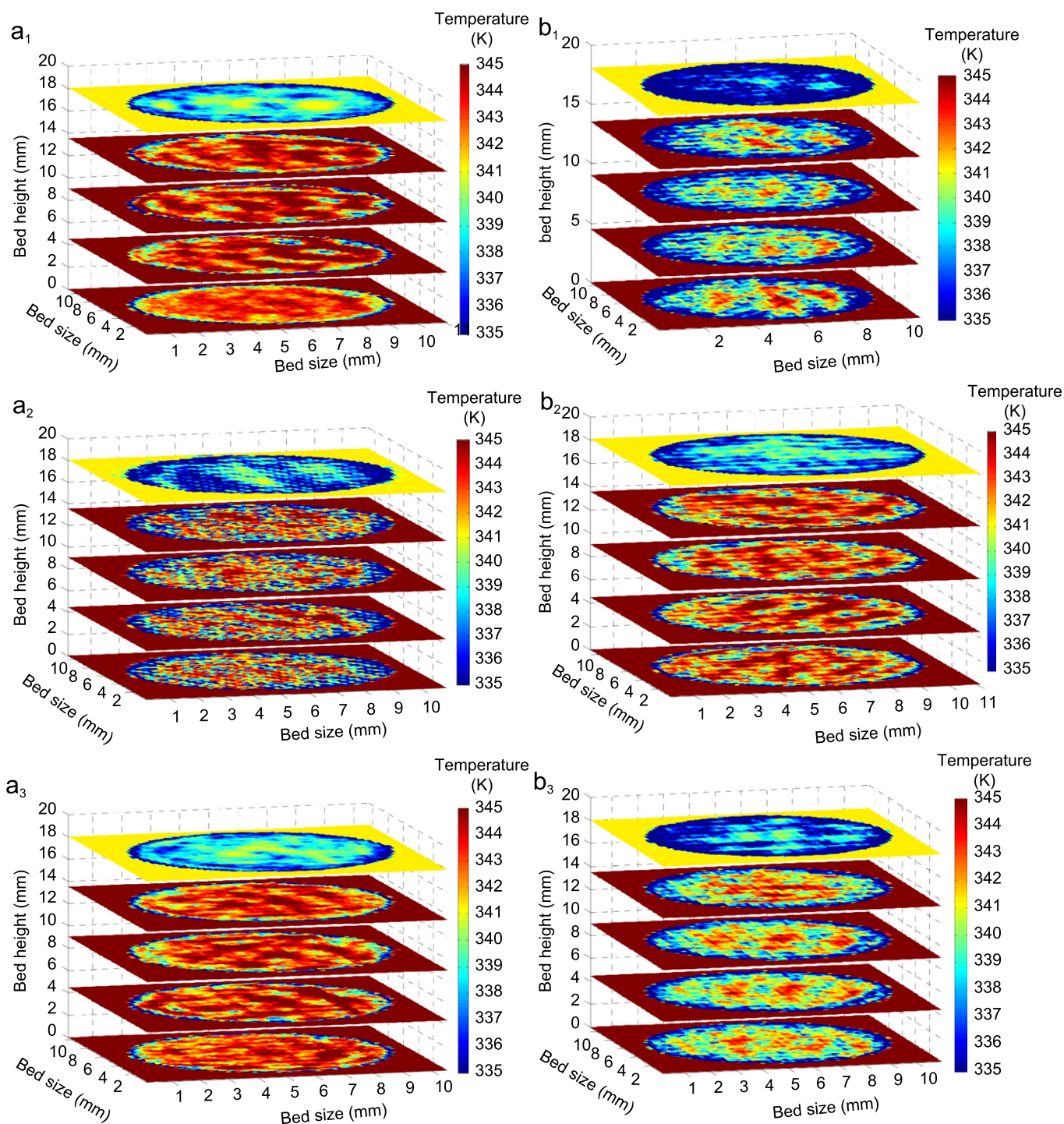


Fig. 14. Wall effect on transient temperature distribution at three aspect ratios of 3 (a1–a3), 9 (b1–b3) and 13 (c1–c3), subscripts 1, 2 and 3 correspond to 5, 60 and 240 min, respectively, packing height: 14 mm, wall temperature: 333 K, water vapour composition: 6.0 mol%, N_2 flow rate: $338 \text{ cm}^3 \text{ min}^{-1}$.

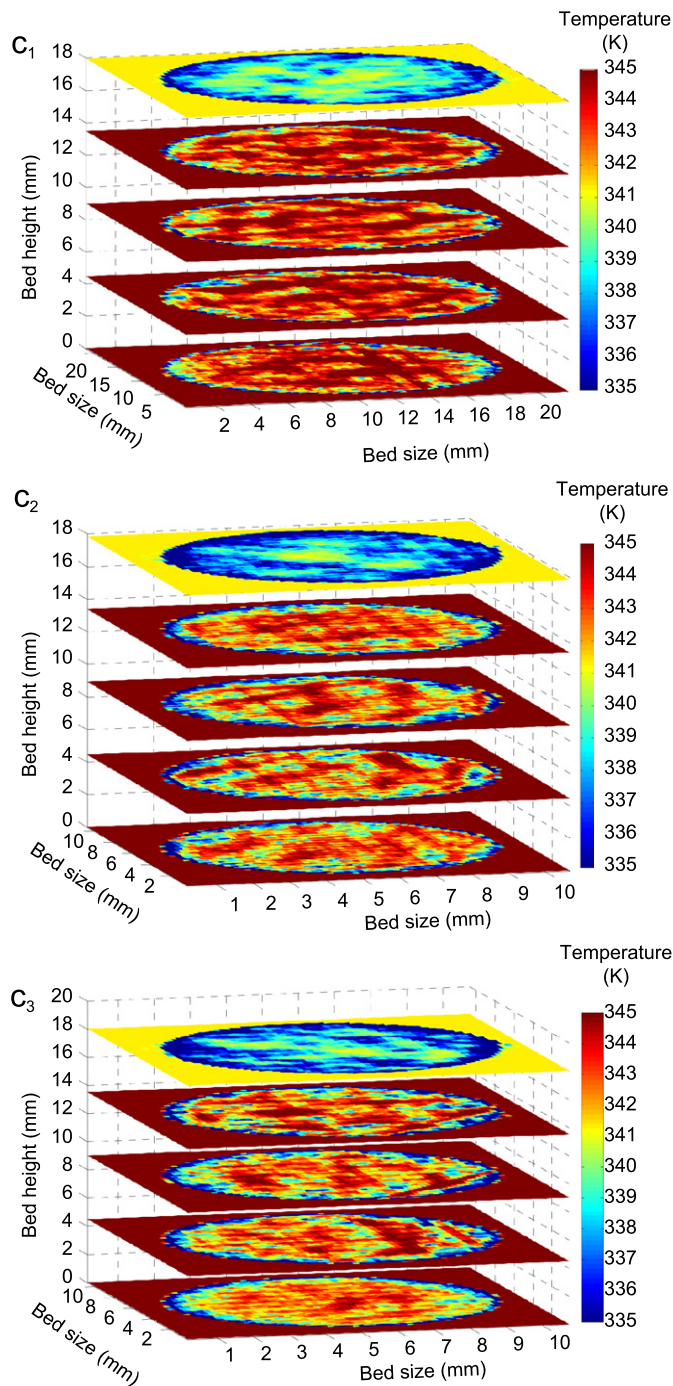


Fig. 14. (continued)

which demonstrates that the maldistribution was present along both radial and angular coordinates. At upper layers of the packing bed, the flow structure warmed up, as observed in the second and the third cross-layers, where hot zones are seen around the centre of the bed, suggesting that the radial flow was minimal in this area, and was therefore unable to release the increase in energy by water vapour adsorption on the silica. A noticeable decrease in temperature can be seen when moving from the packing to the empty space above the packing, as seen in the top cross-section layer, due to inherent lower heat transfer rates in the gaseous phase.

Supplementary material related to this article can be found online at [doi:10.1016/j.ces.2011.08.049](https://doi.org/10.1016/j.ces.2011.08.049).

If uneven hot and cold spots similar to those in the packing remain visible, their distribution tends to decrease towards the wall,

as shown in Fig. 10, which displays a vertical section temperature map through the centre of the bed. A less uniform temperature distribution is seen in the packed region than in the top empty region where hot zones seem to be moving progressively towards the upper regions of the wall according to the parabolic distribution of gas velocity in this region. In addition there is a feature visible on the left-hand side of the vertical section and close to the wall, which shows successive cold and hot zones in the axial direction, leading to a slow flow upwards between the cold and hot zones along the wall, while a displaced upward flow occurred through the neighbouring particle layers towards the centre. The vertical structure of the thermal layer next to the wall is clearly seen. This behaviour implies that local heat transfer varied strongly with local flow pattern in the packed bed.

4.2.1.2. Composition profiles. Unlike structured packing, the present packing, which is eventually a random one, irregularly alternates silica gel particles and porosity along the axial, radial and angular coordinates; this packing (with an aspect ratio of tube to silica gel particle diameters of $Dt/dp=13$) presents radial variation in the porosity due to the relatively larger values in the vicinity of the wall. Fig. 11 shows the composition profiles of five cross-layers along the packed bed, where the four bottom ones belong to the packing phase and the top layer is representative of the breakthrough of gas to the empty section above the packing, at similar conditions to those of Fig. 9 and after an adsorption period of 60 min. Full 700 cross-sectional layers from the bottom to the top of the packed bed were gathered in a movie at a frame rate of 24 layers s^{-1} as shown in the supplementary material (S_2). The composition changes of water vapour in the radial and angular directions were up to 4 mol%. A non-uniform distribution of composition is observed in the packing and the empty section above the packing. High compositions of water vapour are observed near the wall and lower compositions are randomly distributed in the core centre of the bed. These uneven distributions indicate that the local flow is stagnant, circulating and channelling between the silica particles. A closer examination of the composition maps in the packing shows that there is less mixing than in the top empty region where composition maps tend to be moving towards the centre of the tube according to the parabolic shape of the velocity. Fig. 12 shows the vertical cross-section of the composition map through the centre of the tube. One can observe that at a height of 14 mm, which is the top layer of the packing section, the profile of the water vapour is similar to the one prevalent in the neighbouring layers above the packing, with water vapour composition near the wall larger than that at the centre.

Supplementary material related to this article can be found online at [doi:10.1016/j.ces.2011.08.049](https://doi.org/10.1016/j.ces.2011.08.049).

In addition, there are two observations that can be made from the plots about the similarity of the composition profiles of the upper packing and that above the empty section: (1) Radial and reversed flows were present in the whole packing since the upstream flow affected the composition profiles of the downstream flow at the packing–empty section interphase. (2) The gradients of temperature and compositions inside the silica particles, which could indicate internal mass and heat transfer limitations, were not taken into account due to the limited spatial resolution of $0.15 \times 0.026 \text{ mm}^2$. The effect of particle size, aspect ratio and flow rates on the overall flow dynamics are therefore investigated in the following sections.

4.2.2. Effect of aspect ratio and feed flow rates on temperature and composition distributions

4.2.2.1. Effect of aspect ratio. The effect of the wall on flow maldistribution was examined by observing composition profiles with time

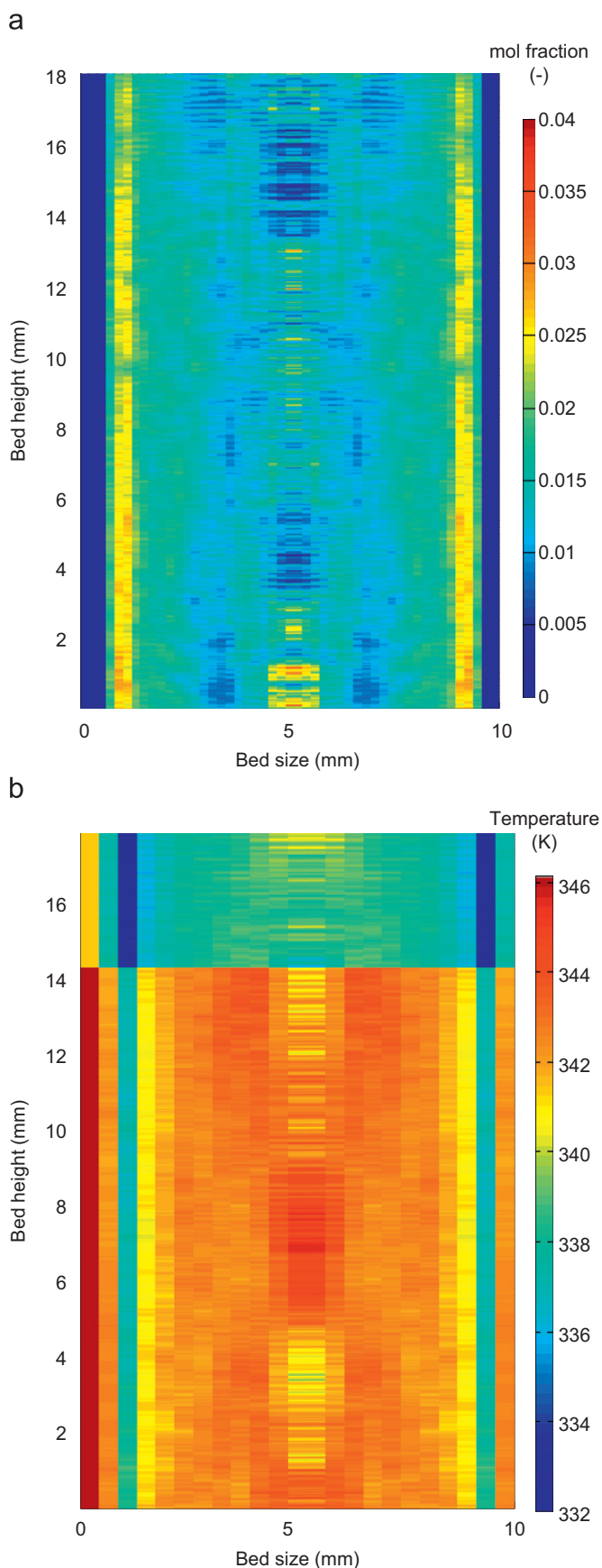


Fig. 15. Transient 2D circumferentially averaged composition and temperature (a) composition and (b) temperature, time: 14 min, packing height: 14 mm, particle size 0.7 mm (AR: 13), wall temperature: 333 K, water vapour composition: 6.0 mol%, N_2 flow rate: $338 \text{ cm}^3 \text{ min}^{-1}$.

at three aspect ratios (AR) of 3, 9 and 13, as shown by Fig. 13(a₁–a₃), (b₁–b₃) and (c₁–c₃), respectively, where subscripts 1–3 represent the time of the experiments, viz., 5, 60 and 240 min adsorption, respectively. After 5 min, as shown by Fig. 13(a₁), (b₁) and (c₁), regardless of the aspect ratio used, the composition maps show a low but pseudo-homogeneous distribution of composition over the five slices of the packing and above the packing, indicating an effective cross-mixing at the start of the water flow, while the temperature maps at this time, as shown by Fig. 14(a₁), (b₁) and (c₁), are homogeneous for an AR of 3 but slightly higher at an AR of 13. After 60 min, however, as shown by Fig. 13(a₂) and (c₂), the water vapour compositions increased for ARs of 3 and 13 and increased still further for an AR of 9, as shown by Fig. 13(b₂), particularly at the wall regions, indicating an efficient cross-mixing. This was confirmed by the corresponding temperature maps, as shown by Fig. 14(a₂) and (c₂), which are higher than those for an AR of 13 (Fig. 14(b₂)), particularly towards the core centre of the packed bed. Thus, the lag in composition between the wall and the core bed increased when the AR increased from 3 to 9, and decreased from an AR of 9 to 13. This profile of composition lags suggest that at an AR of 3 or 9, the adsorption process was dominated more by mass transfer inside the particles where large particle sizes retarded more the flow in the core bed compared with the flow in the wall vicinity. At a particle size of 0.7 mm, which corresponds to an AR of 13 as shown in Fig. 13(c₁–c₃), the small size of the particles and the lag increase suggest an adsorption process dominated by the flow between particles. The temperature maps, however, were only slightly affected by the aspect ratios used. Temperature maps are higher at the core of the bed than at the wall for ARs of 3 and 9, but more homogeneous with an AR of 13, suggesting that the convective transfer, which was dominant near the wall with low AR due to its high porosity, was less effective at a high aspect ratio. This result agrees with those of Aris (1975) and Yang (1997) on zeolite packed beds of similar porosity and thermal conductivity, where major resistances for mass and heat transfers were found inside and outside (interphase) particles of size above 1 mm, respectively. After 240 min, Fig. 13(a₃), (b₃) and (c₃) shows uneven composition maps associated with high values in the near-wall regions, which suggest that the wall effect on water vapour flow was significant, particularly for the packed bed with an AR of 9. The temperature profiles, as shown in Fig. 14(a₃), (b₃) and (c₃), are roughly similar for AR equal to 9 and 13, and more pronounced than those at AR equal to 3.

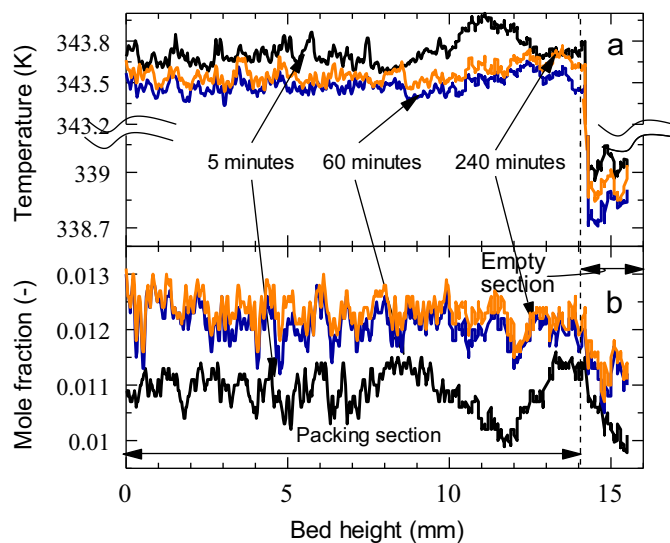


Fig. 16. Transient 1D circumferentially and radially averaged composition and temperature (a) temperature (b) composition, packing height: 14 mm, particle size: 0.7 mm (AR: 13), wall temperature: 333 K, water vapour composition: 6.0 mol%, N_2 flow rate: $338 \text{ cm}^3 \text{ min}^{-1}$.

These results of the 3D distribution of temperature and compositions NIRDTT at three aspect ratios agree with the overall behaviour of the gas flow in low aspect ratio packed beds, that is (1) at the lowest aspect ratio (i.e., an AR of 3), the flow maldistribution in the vicinity of the wall and the slow in-particle mass transfer caused quiescent radial cross-mixing; (2) at the intermediate value of AR (i.e., an AR of 9), the water vapour composition in the core remained smaller than the near-wall one, in which case the effect of maldistribution and in-particle mass transfer dominated and (3) at the highest AR (i.e., 13), the maldistribution decreased, leading a slight lag in water vapour flow between the core and the near-wall regions and improved radial cross-mixing.

Averaged composition and temperature profiles along axial, radial or circumferential (angular) coordinates are of a great

interest in modelling chemical processes using 2D and 1D models since 3D modelling is still complex and sometimes impractical in terms of computation time. The 3D distributions of composition and temperature shown in Figs. 13(b₂) and 14(b₂) were reduced to 2D circumferentially averaged composition and temperature as shown in Fig. 15(a) and (b), respectively. These two figures clearly show the effect of the wall on the flow maldistribution associated with the high composition of water vapour near the wall and a damped one towards the core of the packed bed, whereas there is a significant increase of temperature in the core bed of the packed bed adsorber. The composition profiles along the radial direction correlate well with general trends of porosity profiles in low aspect ratio packed beds. Along the axial direction, however, the composition profile was not uniform in the core bed

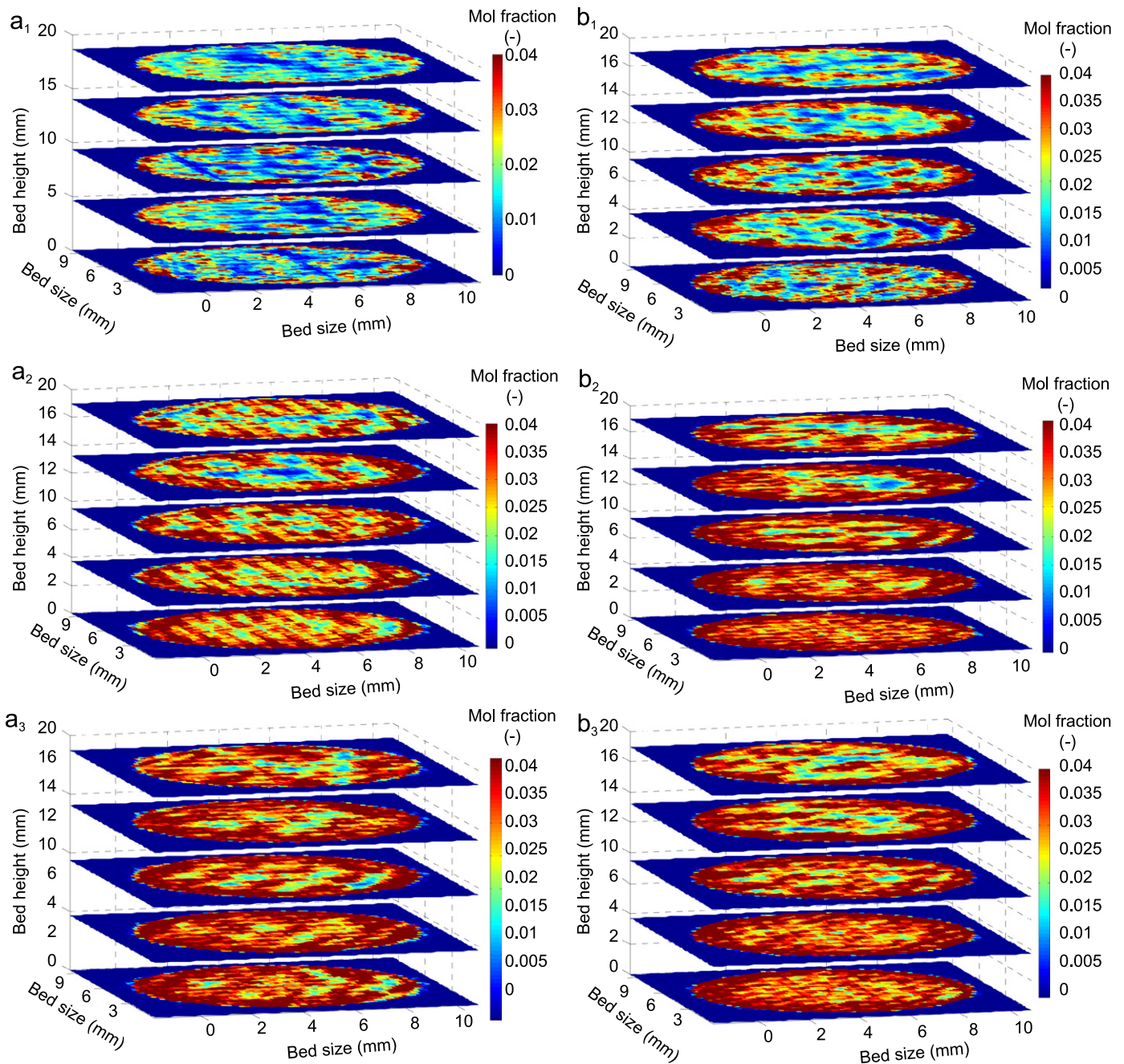


Fig. 17. Effect of flow rate on composition distribution of water vapour at aspect ratio of 9, a₁–a₃: 74 cm³ min⁻¹, b₁–b₃: 170 cm³ min⁻¹ and c₁–c₃: 338 cm³ min⁻¹, subscripts 1, 2 and 3 correspond to 5, 60 and 240 min, respectively, packing height: 14 mm, particle size: 0.7 mm (AR: 13), wall temperature: 333 K, water vapour composition: 6.0 mol%.

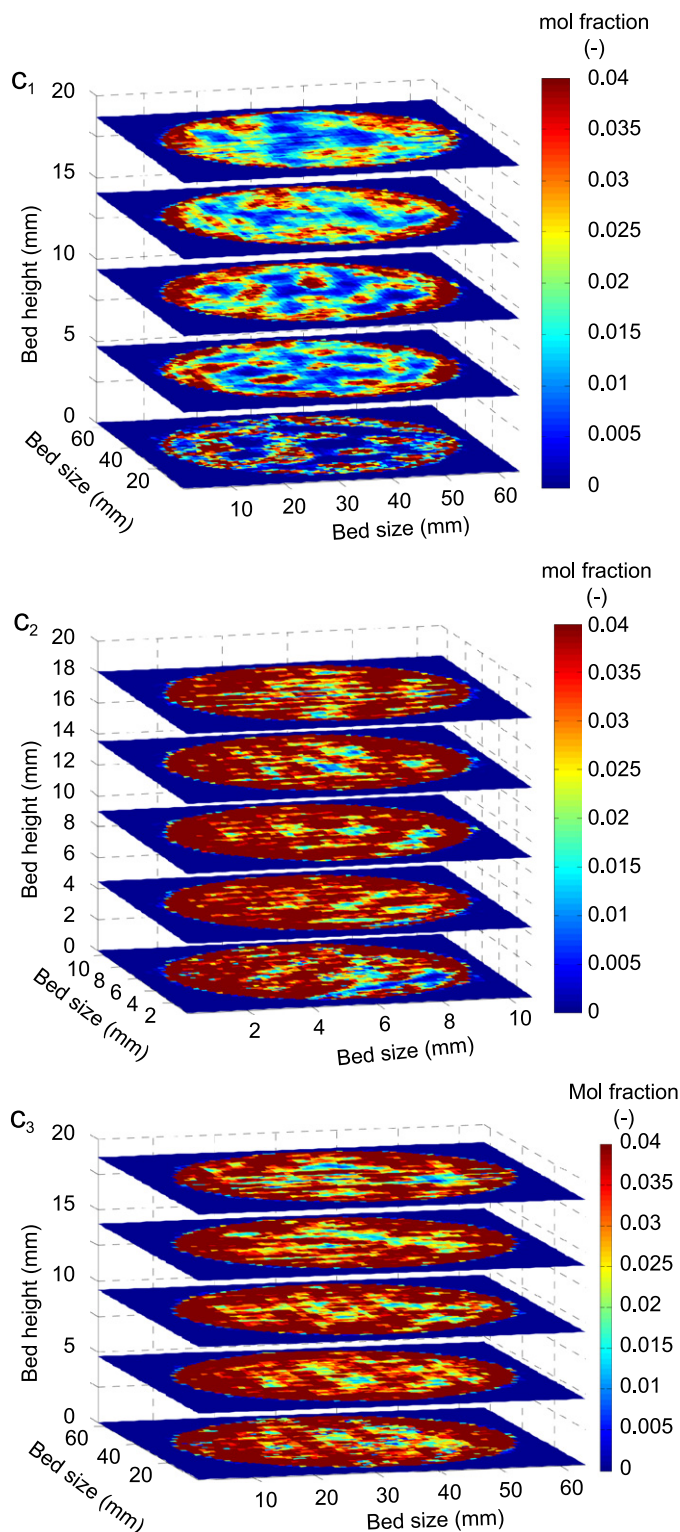


Fig. 17. (continued)

and, therefore, was affected significantly by the random arrangement of the packed bed.

The 3D distributions of composition and temperature shown in Figs. 13(b₁–b₂) and 14(b₁–b₃) were reduced to 1D circumferentially- and radially-averaged temperature and composition as shown in Fig. 16(a) and (b), respectively. Steady values of temperature are shown along the axial direction at anytime of the experiment and up to the section above the packing where an average drop in

temperature of 5 K occurred. The composition profile, however, shows an uneven distribution along the axial direction after 5 min adsorption where the packing arrangement was effective on flow cross-mixing as observed in Fig. 13(b₁). Further adsorption times show steady values of compositions along the height of the packed bed and an averaged decrease from the inlet to the empty section above the packing of 35 mol% m⁻¹.

4.2.2.2. Effect of flow rate. The effect of the wall on the flow maldistribution of water vapour was examined by observing composition profiles with time at an AR of 13 (negligible internal mass transfer resistance) and three flow rates of 74, 170 and 338 cm³ min⁻¹, as shown by Fig. 17(a₁–a₃), (b₁–b₃) and (c₁–c₃), respectively. At the lowest flow rate, as shown by Fig. 17(a₁–a₃), the contribution of cross-mixing decreased as the visible extent of the near-wall channelling is higher than in Fig. 17(b₁–b₃) and (c₁–c₃), where higher flow rates were used. At these high flow rates, more homogeneous composition distributions and less lag between the centre of the packing and the near-wall regions were observed. The temperature profiles that correspond to the three flow rates are shown in Fig. 18(a₁–a₃), (b₁–b₃) and (c₁–c₃). Increasing the water vapour flow rate promoted less heat transfer from the packed bed to the cooling wall, which suggests that the convective contribution to effective heat transfer was not important at the flow rates used.

It is interesting to note that 3D imaging by NIRDIT of fluid flow in a packed bed of silica gel allowed the water vapour composition near the wall and a higher temperature towards the core centre to be discernible when a low aspect ratio was used. The flow maldistribution was a complex interplay between different phenomena. The flow maldistribution was the result of fluid flow in bed porous media, which was uneven at small aspect ratios, but also it was the result of the mass transfer effect inside the packing particles and adsorption equilibrium. An ongoing study is currently using resin copolymer as catalyst where the macro-porosity and low thermal conductivity lead to flow dynamics at reduced in-particle thermal and mass transfer limitations.

5. Conclusions

This study, which is the first on gas flow visualization in porous media using optical tomography, demonstrated that NIRDIT can be applied to examine the actual behaviour of flowing gases by measuring the 3D distribution of composition and temperature in a weakly scattering environment. The 2D projected images from parallel scanning permitted data to be retrieved from the packing and above the packing sections (12.0 × 12.0 × 18.2 mm³) at a volume-resolution of 0.15 × 0.15 × 0.026 mm³ and a time-resolution of less than 3 min. The relative deviations in temperature and compositions were 11.1% and 9.3%, respectively. This deviation in composition, which covers the packing and above the packing sections, is slightly higher than the deviation of 8% obtained by Salem et al. (2005), which was limited to the exit of a packed bed adsorber.

Several design limitations inherently associated with optical tomography were either reduced or suppressed such as (1) water vapour was used as the tracer due to its high absorption coefficient in NIR. The extension to common gases such as CO, CO₂ and NO_x, which are known to exhibit low absorption coefficients compared to water, is ongoing using a suitable design to promote the optical path and make NIRDIT sensitive to low compositions; (2) wall transparency and deflection were taken into account using a highly transparent glass of small thickness. Larger thicknesses that would be convenient to higher pressure flow require the additional design of the ray geometry to be taken into account for the tomography reconstruction; (3) in addition,

a camera highly sensitive to the low intensity light exiting the packed bed was used.

The maldistribution was not only affected by the bed porosity but also by the packing size and flow dynamics. At the lowest flow rate, the contribution of cross-mixing decreased as the visible extent of the damped zone was larger. Increasing the water vapour flow rate, however, slightly promoted heat transfer from the packing to the wall.

Flow maldistribution was observed in a packed bed of AR of 13 (i.e., particle size of 0.7 mm), inlet and wall temperatures of 333 K,

flow rate of 338 ml min^{-1} and water vapour composition of 6 mol%. A lag between the near-wall flow and the core bed flow was clearly observed at the lowest aspect ratio used (i.e., an AR of 3) where flow maldistribution and internal mass transfer dominated, while temperature distribution was unevenly distributed and higher at the centre of the packed beds due to the exothermicity of adsorption process. The temperature maps, however, have been slightly affected by the aspect ratios used, suggesting that the convective transfer, which was dominant near the wall with low AR due to high porosity, was also effective at high aspect ratios.

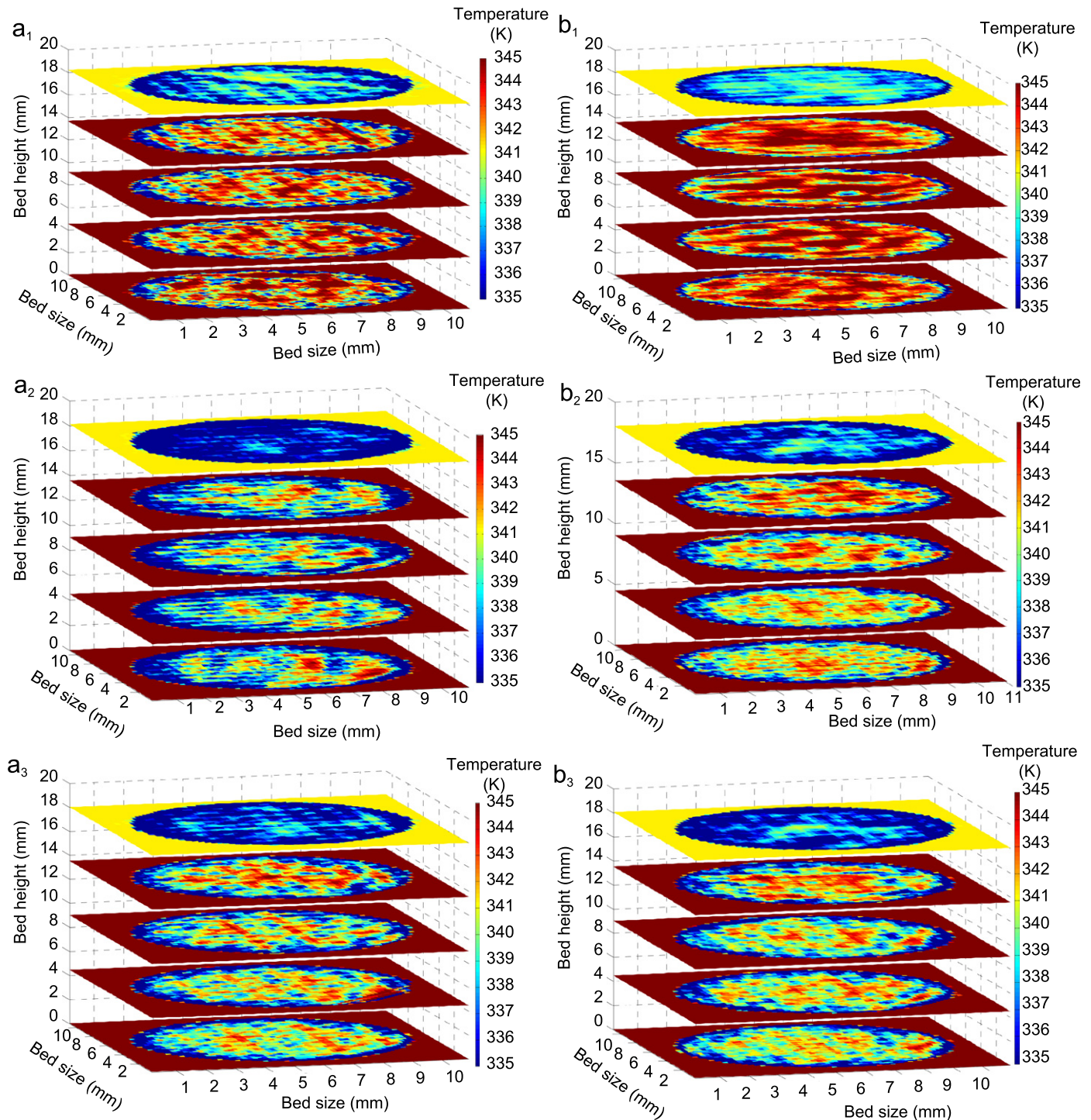


Fig. 18. Effect of flow rate on temperature distribution at aspect ratio of 9, a_1 – a_3 : $74 \text{ cm}^3 \text{ min}^{-1}$, b_1 – b_3 : $170 \text{ cm}^3 \text{ min}^{-1}$ and c_1 – c_3 : $338 \text{ cm}^3 \text{ min}^{-1}$, subscripts 1, 2 and 3 correspond to 5, 60 and 240 min, respectively, packing height: 14 mm, particle size: 0.7 mm (AR: 13), wall temperature: 333 K, water vapour composition: 6.0 mol%.

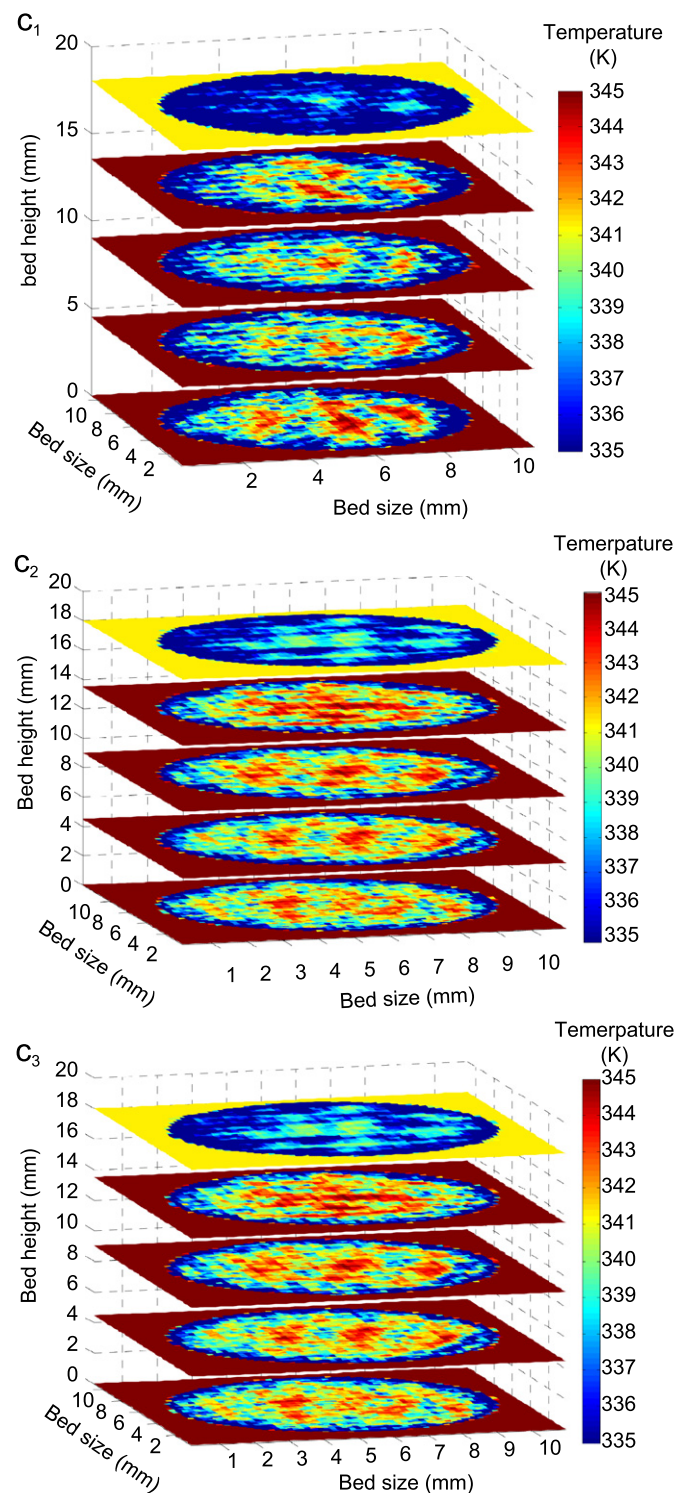


Fig. 18. (continued)

Nomenclature

| | |
|------------|-----------------------------------------------------------------|
| <i>Abs</i> | integral absorbance, dimensionless |
| <i>C</i> | mole fraction of water vapour across the packing, dimensionless |
| <i>c</i> | speed of light, m s^{-1} |
| <i>E</i> | lower state energy, cm^{-1} |
| <i>f</i> | object function, K or dimensionless |
| <i>h</i> | Planck's constant, J s |

| | |
|-------------|-------------------------------------------------------------------------------------|
| <i>k</i> | Boltzmann's constant, J K^{-1} |
| <i>l</i> | optical path length, cm |
| I_λ | absorption intensity at wavelength λ , $\text{cm}^{-2} \text{atm}^{-1}$ |
| <i>M</i> | total number of voxels, dimensionless |
| <i>N</i> | total number of projection rays, dimensionless |
| <i>Q</i> | temperature-dependent partition function of water vapour, dimensionless |
| <i>R</i> | integral absorbance ratio, dimensionless |
| <i>S</i> | line strength of temperature-dependent transition, $\text{cm}^{-2} \text{atm}^{-1}$ |
| <i>T</i> | water vapour temperature, K |

Greek symbols

| | |
|---------------|---------------------------------------------------------|
| ε | absorption coefficient, $\text{atm}^{-1} \text{m}^{-1}$ |
| φ | line shape function, cm |
| <i>w</i> | weighting factor, dimensionless |
| λ^i | relaxation parameter, dimensionless |

Abbreviations

| | |
|--------|---------------------------------------------|
| MRI | magnetic resonance imaging |
| NIRDTT | diffuse transmittance tomography |
| NIR | near-infrared |
| FPA | focal planar array |
| AART | adaptive algebraic reconstruction technique |

Acknowledgements

The authors would like to thank the Department of Education and Learning (DEL) for the financial support and Mrs. P. Marr for the technical support with the silica gel.

References

- Aris, R., 1975. *The Mathematical Theory of Diffusion and Reaction in Permeable Catalysts*, vol. 1—The Theory of Steady State. Clarendon Press, Oxford, UK.
- Arridge, S.R., Dehghani, H., Schweiger, M., 2000. The finite element model for the propagation of light in scattering media: a direct method for domains with non scattering regions. *Med. Phys.* 27, 252–264.
- Asano, H., Nakajima, T., Takenaka, N., Fujii, T., 2005. Visualization of the hygroscopic water distribution in an adsorbent bed by neutron radiography. *Nucl. Instrum. Methods—Phys. Res. A* 542, 241–247.
- Cai, C.B., Han, Q.J., Tang, L.J., Xu, L., Jiang, J.H., Wu, H.L., Yu, R.Q., 2009. Studying the uptake of aniline vapour by active alumina through in line monitoring a differential adsorption bed with near-infrared diffuse reflectance spectroscopy. *Adsorption—J. Intern. Adsorption Soc.* 15, 23–29.
- Carey, S.J., McCann, H., Hindle, F.P., Ozanyan, K.B., Winterbone, D.E., Clough, E., 2000. Chemical species tomography by near infra-red absorption. *Chem. Eng. J.* 77, 111–118.
- Coppens, M.-O., 2005. Scaling-up and -down in a nature-inspired way. *Ind. Eng. Chem. Res.* 14, 5011–5019.
- Dyakowski, T., Jaworski, A., 2003. Non-invasive process imaging—principles and applications of industrial process tomography. *Chem. Eng. Technol.* 26, 697–706.
- Freund, H., Bauer, J., Zeiser, T., Emig, G., 2005. Detailed simulation of transport processes in fixed-beds. *Ind. Eng. Chem. Res.* 44, 6423–6434.
- Goguet, A., Burch, R., Chen, Y., Hardacre, C., Hu, P., Joyner, R.W., Meunier, F.C., Mun, B.S., Thompsett, A., Tibiletti, D., 2007. Deactivation mechanism of a Au/CeZrO₄ catalyst during a low-temperature water gas shift reaction. *J. Phys. Chem. C* 111, 16927–16933.
- Hindle, F., Carey, S., Ozanyan, K., Winterbone, D., Clough, E., McCann, H., 2001. Measurement of gaseous hydrocarbon distribution by a near infra-red absorption tomography system. *J. Electron. Imaging* 10, 593–600.
- Lindstrom, T.H., Tsotsis, T.T., 1986. Reaction rate oscillations during CO oxidation over Pt/ γ -Al₂O₃: the issue of propagating waves. *Surf. Sci.* 167, L194–L202.
- Ma, L., Cai, W., Caswell, A.W., Kraetschmer, T., Sanders, S.T., Roy, S., Gord, J.R., 2009. Tomographic imaging of temperature and chemical species based on hyperspectral absorption spectroscopy. *Opt. Express* 17, 8602–8613.
- Magnico, P., 2009. Pore-scale simulations of unsteady flow and heat transfer in tubular fixed beds. *AIChE J.* 55, 849–867.

- Nadeau, P., Berk, D., Munz, R.J., 1996. Measurement of residence time distribution by laser absorption spectroscopy. *Chem. Eng. Sci.* 51, 2607–2612.
- Nijemeisland, M., Dixon, A.G., Stitt, E.H., 2004. Catalyst design by CFD for heat transfer and reaction in steam reforming. *Chem. Eng. Sci.* 59, 5185–5191.
- Nijemeisland, M., Dixon, A.G., 2004. CFD study of fluid flow and wall heat transfer in a fixed bed of spheres. *AIChE J.* 50, 5–14.
- Reinke, M., Mantzaras, J., Bombach, R., Schenker, S., Inauen, A., 2005. Gas phase Chemistry in catalytic combustion of methane/air mixtures over platinum at pressures of 1 to 16 bars. *Combust. Flame* 141, 448–468.
- Rigby, S.P., Gladden, L.F., 1996. NMR and fractal modelling studies of transport in porous media. *Chem. Eng. Sci.* 51, 2263–2272.
- Roels, S., Carmeliet, J., 2006. Analysis of moisture flow in porous materials using microfocus X-ray radiography. *Int. J. Heat Mass Transfer* 49, 4762–4772.
- Rothman, L.S., Gordon, I.E., Barbe, A., Chris Benner, D., Bernath, P.F., Birk, M., Boudon, V., Brown, L.R., Campargue, A., Champion, J.-P., Chance, K., Coudert, L.H., Dana, V., Devi, V.M., Fally, S., Flaud, J.-M., Gamache, R.R., Goldman, A., Jacquemart, D., Kleiner, I., Lacombe, N., Lafferty, W.J., Mandin, Y.-J., Massie, S.T., Mikhailenko, S.N., Miller, C.E., Moazzen-Ahmadi, N., Naumenko, O.V., Nikitin, A.V., Orphal, J., Perevalov, V.I., Perrin, A., Predoi-Cross, A., Rinsland, C.P., Rotger, M., Simčková, M., Smith, M.A.H., Sung, K., Tashkun, S.A., Tennyson, J., Toth, R.A., Vandaele, A.C., VanderAuwera, J., 2009. The HITRAN 2008 molecular spectroscopic database. *J. Quant. Spectrosc. Radiat. Transfer* 110, 533–572.
- Sa, J., Fernandes, D.L.A., Aiouache, F., Goguet, A., Hardacre, C., Lundie, D., Naeem, W., Partridge, W.P., Stere, C., 2010. SpaciMS: spatial and temporal operando resolution of reactions within catalytic monoliths. *Analyst* 135, 2260–2272.
- Salem, K., Tsotsas, E., Mewes, D., 2005. Tomographic measurement of breakthrough in a packed bed adsorber. *Chem. Eng. Sci.* 60, 517–522.
- Shao, J., Lathdavong, L., Kluczynski, P., Lundqvist, S., Axner, O., 2009. Methodology for temperature measurements in water vapor using wavelength-modulation tunable diode laser absorption spectrometry in the telecom C-band. *Appl. Phys. B: Lasers Opt.* 97, 727–748.
- Son, I.H., 2003. The study of the deactivation of water-pretreated Pt/gamma-Al₂O₃ for low-temperature selective CO oxidation in hydrogen. *J. Power Resour.* 124, 415–419.
- Terzija, N., Davidson, J.L., Garcia-Stewart, C.A., Wright, P., Ozanyan, K.B., Pegrum, S., Litt, T.J., McCann, H., 2008. Image optimization for chemical species tomography with an irregular and sparse beam array. *Meas. Sci. Technol.* 19, 1–13.
- Tsakoumis, N.E., Ronning, M., Borg, O., Rytter, E., Holmen, A., 2010. Deactivation of cobalt based Fischer-Tropsch catalysts: a review. *Catal. Today* 154, 162–182.
- Urakawa, A., Baiker, A., 2009. Space-resolved profiling relevant in heterogeneous catalysis. *Top. Catal.* 52, 1312–1322.
- Weckhuysen, B.M., 2009. Chemical imaging of spatial heterogeneities in catalytic solids at different length and time scales. *Angew. Chem. Int. Ed.* 48, 4910–4943.
- Yang, D.M., He, P.K., Dong, F., 2006. Effect of water vapor at room temperature on photocatalytic decomposition of gaseous ozone over Au/TiO₂. *Chin. J. Catal.* 27, 1122–1126.
- Yang, R.T., 1997. *Gas Separation by Adsorption Processes*. World Scientific Publishing Co. Inc., Imperial College, UK.
- Zhou, X., Liu, X., Jeffries, J.B., Hanson, R.K., 2003. Development of a sensor for temperature and water concentration in combustion gases using a single tunable diode laser. *Meas. Sci. Technol.* 14, 1459–1468.